Journal of Materials Research and Technology 38 (2025) 4016–4026

Contents lists available at ScienceDirect

Journal of Materials Research and Technology

journal homepage: www.elsevier.com/locate/jmrt

# The effect of initial microstructure on the irradiation hardening of the W fiber in $W_f/W–Y_2O_3$ composites

C. Chen [a,b], J.H. Chen [a], Y. Chen [a], J. Wang [a,*], Y.F. Zhang [a], S. Wang [a,c,**], H.Y. Chen [d], Y.R. Mao [e], L.M. Luo [a,b]

[a] School of Materials Science and Engineering, Hefei University of Technology, Hefei, 230009, China
[b] Engineering Research Center of High-Performance Copper Alloy Materials and Processing, Ministry of Education, Hefei University of Technology, Hefei, 230009, China
[c] Anhui Province Key Lab of Aerospace Structural Parts Forming Technology and Equipment, Hefei University of Technology, Hefei, 230009, China
[d] College of Mechanical Engineering, Zhejiang University of Technology, Hangzhou, 310023, China
[e] Institut für Energie und Klimaforschung-Plasmaphysik, Forschungszentrum Jülich GmbH, Jülich, 52425, Germany

ARTICLE INFO

*Keywords:*
Tungsten fiber-reinforced tungsten composites
Helium ion irradiation
Nanoindentation
Irradiation hardening

ABSTRACT

Tungsten fiber-reinforced tungsten ($W_f/W$) composites are promising candidates for plasma facing materials for fusion devices. The hardening behaviors of unrecrystallized W fiber (NRX-W fiber) and fully recrystallized W fiber (RX-W fiber) in the $W_f/W–Y_2O_3$ composites after helium ion irradiation (180 keV) were studied. The results reveal that the lattice distortion and microscopic residual stress in both the NRX-W fiber and the RX-W fiber increase after irradiation. The observation of dislocation loops with lower number density and smaller size in the NRX-W fiber compared to the RX-W fiber indicates that the NRX-W fiber has an enhanced capacity for capturing irradiation-induced defects. This enhanced capacity arises from its characteristics, including an initially larger proportion of high-angle grain boundaries (HAGBs), a higher density of subgrain boundaries, and geometrically necessary dislocations (GNDs). Nanoindentation tests show that the irradiation hardening increments for NRX-W fiber and RX-W fiber are 4.38 ± 0.10 GPa and 5.08 ± 0.17 GPa, respectively. Notably, the irradiation hardening rate of NRX-W fiber is 52.96 %, which is significantly lower than that of RX-W fiber (84.95 %), indicating superior resistance to helium ion irradiation hardening in the NRX-W fiber. Consistent with these experimental findings, theoretical calculations using the dispersed barrier hardening (DBH) model yield irradiation hardening increments of 3.68 GPa and 4.99 GPa for NRX-W fiber and RX-W fiber, respectively. Additionally, dislocation loops exhibit a uniform distribution within the equivalent crystallographic orientation, with their contributions being dominant in the irradiation hardening of both fiber types.

## 1. Introduction

Tungsten fiber-reinforced tungsten ($W_f/W$) composites have become important candidates for plasma-facing materials in fusion reactors due to their excellent thermal shock resistance and fracture toughness [1,2]. However, during the preparation of the composites or their high-temperature service, the recrystallization of the W fiber is inevitable, leading to the coarsening and annihilation of their initial high-density defect structures (such as high-angle grain boundaries, subgrain boundaries, and geometrically necessary dislocations) [3–7]. Notably, as plasma-facing materials, the $W_f/W$ composites will be exposed to high-flux neutron irradiation during the operation of fusion reactors, inducing a large number of irradiation defects (such as dislocation loops and helium bubbles) [8]. The evolution behavior of these defects is highly dependent on the material's initial microstructure. The reduction in defect density caused by recrystallization will affect the ability to capture irradiation defects, thereby changing the irradiation hardening behavior of the material and ultimately influencing its mechanical properties and service life [9,10]. Therefore, revealing the defect evolution laws and their contributions to hardening of recrystallized W fiber (RX-W fiber) and unrecrystallized W fiber (NRX-W fiber) under irradiation conditions is a key prerequisite for clarifying the irradiation damage mechanism of the W fiber in $W_f/W–Y_2O_3$ composites.

* Corresponding author.
** Corresponding author. School of Materials Science and Engineering, Hefei University of Technology, Hefei, 230009, China.
*E-mail addresses:* jwang@hfut.edu.cn (J. Wang), swang@hfut.edu.cn (S. Wang).

https://doi.org/10.1016/j.jmrt.2025.08.233
Received 10 June 2025; Received in revised form 31 July 2025; Accepted 26 August 2025
Available online 26 August 2025

Irradiation behavior in $W_f/W–Y_2O_3$ composites has rarely been reported and the current research is almost focused on the preparation and mechanical properties of $W_f/W$ composites [11–16]. The mechanism of irradiation hardening in conventional W materials is generally well understood. In the case of pure W irradiated with neutrons, dislocation loops and vacancy-type defects dominate the hardening at low doses, while precipitation plays a dominant role at high doses [17]. Due to the long experiment period caused by the activation of the sample after neutron irradiation, the irradiation hardening of pure W has been widely studied by using ion irradiation as an effective method to simulate neutron irradiation [18,19]. W materials with ultrafine grains or nanograins have good radiation resistance due to high grain boundary density [20]. In addition, previous studies have shown that recrystallization W exhibits a greater irradiation hardening effect than the as-received W [21]. This indicates that the grain size has a significant impact on the irradiation hardening behavior. However, as the toughening phase of $W_f/W–Y_2O_3$ composites, the initial microstructure of W fiber, such as the texture, dislocation density and grain size, is quite different from that of conventional W materials, and their evolutionary behavior will also significantly affect the properties of $W_f/W–Y_2O_3$ composites. Therefore, the irradiation hardening behavior of W fiber needs further study.

In this study, the $W_f/W–Y_2O_3$ composites with different initial microstructures were prepared by spark plasma sintering (SPS) at different temperature. And the initial microstructure of $W_f/W–Y_2O_3$ composites was characterized using electron backscattering diffraction (EBSD). All the composites were irradiated with 180 keV He ions at room temperature. The microstructure evolution of the composites after irradiation is analyzed using grazing incidence X-ray diffraction (GIXRD) and transmission electron microscopy (TEM). The associated hardness changes of irradiated W fiber were investigated by nanoindentation tests.

## 2. The materials and experimental procedures

### 2.1. Material preparation

A novel chemical approach was employed to synthesize $W–Y_2O_3$ powder with a $Y_2O_3$ content of 0.5 vol%. The raw materials used were ammonium *para*-tungstate (APT, purity: ≥99.95 %) and yttrium nitrate hexahydrate ($Y(NO_3)_3•6H_2O$, purity: ≥99.5 %). These two chemicals were first dissolved in deionized water to prepare a transparent solution. Subsequently, oxalic acid ($C_2H_2O_4•2H_2O$) was added to induce precipitation of the solution. The resulting mixture was then placed in a methyl silicone oil bath maintained at 185 °C, where it was kept until the precursor was formed. After grinding, the precursor was transferred to a tubular furnace and subjected to reduction using high-purity hydrogen [22]. The short W fiber with potassium doping (75 ppm) was provided by Xiamen Honglu Tungsten and Molybdenum Industry Co., Ltd. The length of the W fiber is 2.4 ± 0.4 mm, and the diameter is 150 μm. The micrographs of the W-0.5 $\%Y_2O_3$ powder and the W fiber are shown in Fig. 1. Fig. 2 shows the distribution of $Y_2O_3$ in the W powder analyzed by energy dispersive spectroscopy (EDS), which was uniformly distributed in the W powder.

The short W fiber and the W-0.5 $\%Y_2O_3$ powder with a volume ratio of 4 : 6 were mixed for 5 h using a three-dimensional mixer, and then placed in a graphite mold. The $W_f/W–Y_2O_3$ composites were prepared by using the spark plasma sintering system (SINTERLAND, LABOX-350). The samples were heated at a rate of 100 °C/min to 1600 °C and 1800 °C under vacuum conditions. The maximum sintering pressure for all samples was 40 MPa, and the holding time was 5 min. The detailed processing parameter of the $W_f/W–Y_2O_3$ composites can be seen in Ref. [16]. A cylindrical material with a diameter of 20 mm and a thickness of approximately 7 mm was finally obtained.

The irradiation samples with dimensions of 10 mm (l) × 10 mm (w) × 1 mm (h) were machined from the SPS sintered samples using a wire-cutting machine. All samples were successively polished with SiC sandpapers of 320#, 800#, 1500# and 4000# to remove any visible scratches on the surface, and then polished with a water-soluble diamond polishing paste of 2.5W to obtain a bright and scratch-free mirror surface. After that, the samples were corroded by using solution of $K_3[Fe(CN)_6]$ (5 g) + NaOH (5 g) + deionized water (50 ml).

### 2.2. Ion irradiation

All the $W_f/W–Y_2O_3$ composites were irradiated with 180 keV He ions at room temperature using the BNU400 ion implanter at Beijing Normal University, China. The beam current measured 100 μA, with a fluence of $1 \times 10^{17}$ ions/cm$^2$. During irradiation, the vacuum chamber's background pressure was around $10^{-4}$ Pa. The dose rate was $3 \times 10^{13}$ ions/(cm$^2$·s) and the duration was 50 min. Temperature was regulated via water cooling at approximately 300 K, maintaining a control accuracy of ±1 K. The damage profile and ion distribution were calculated by using the SRIM software (SRIM-2008.04) [23] with the "Quick Kinchin-Pease mode" [24]. According to ASTM-Standard E512 [25], the displacement threshold energy of W was set at Ed = 90 eV. Fig. 3 shows the depth profiles of displacement per atom (dpa) and implanted He ions. The simulation results revealed that the maximum damage peak of 1 dpa is located at 320 nm. The displace depth and ion range are estimated at approximately 600 nm, and the maximum He concentration is 6 at.%.

### 2.3. Microstructure characterization

The microstructures of the W fiber were evaluated by optical microscope (Zeiss Axio Lab A, OM), electron backscatter diffraction detector (Oxford AZtec, EBSD), and grazing incidence X-ray diffraction (D/MAX2500VL/PC, GIXRD). The sample for EBSD detection was a block of 3 mm (l) × 3 mm (w) × 2 mm (h) fabricated by a wire-cutting machine. After mechanical polishing the block sample to a smooth mirror surface, an Argon ion polishing instrument (Gatan Inc. 697. C) was used to remove the residual stress on the test surface of the sample. The crystal structure of the samples before and after irradiation was characterized by GIXRD of Cu Kα radiation. Based on the simulation of the SRIM software, the damage depth was evaluated to be 600 nm. Consequently,

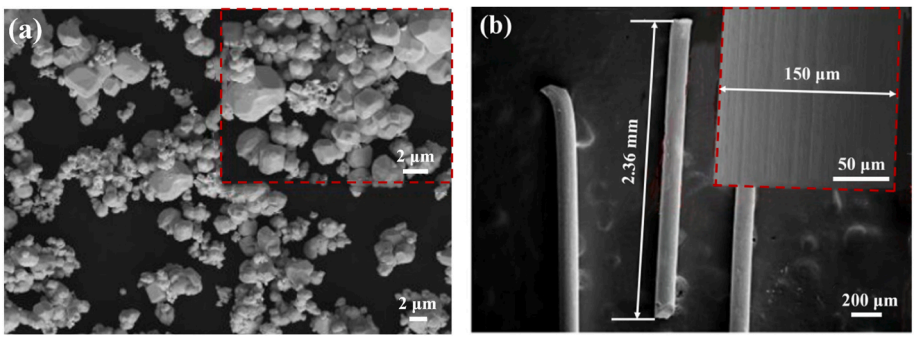


**Fig. 1.** SEM images showing the morphology of (a) the W-0.5 $\%Y_2O_3$ powder and (b) the W fiber.

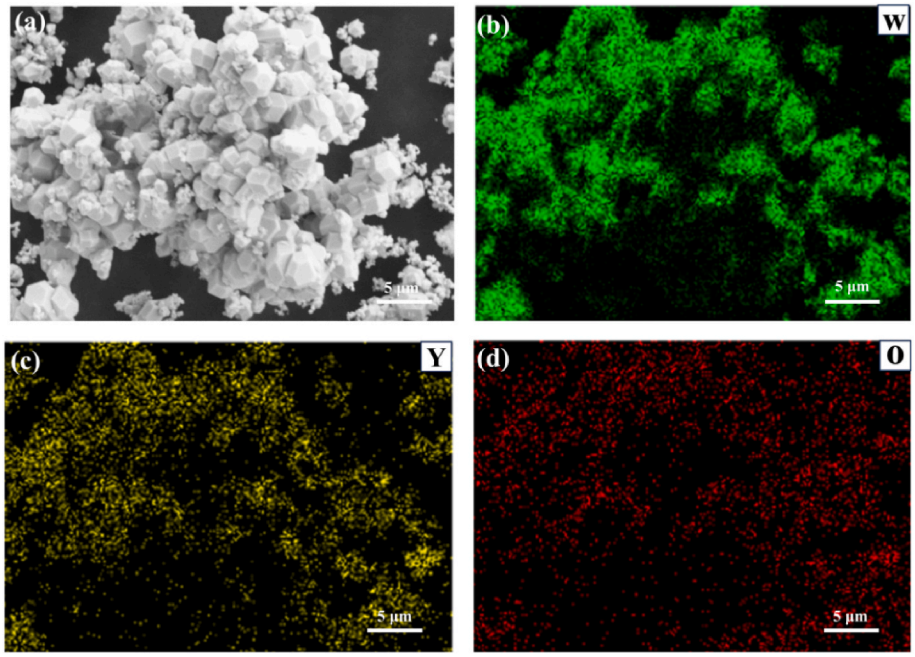


**Fig. 2.** (a) The morphology of W-0.5 %$Y_2O_3$ powder and the corresponding elemental distribution maps of (b) W, (c) Y and (d) O.

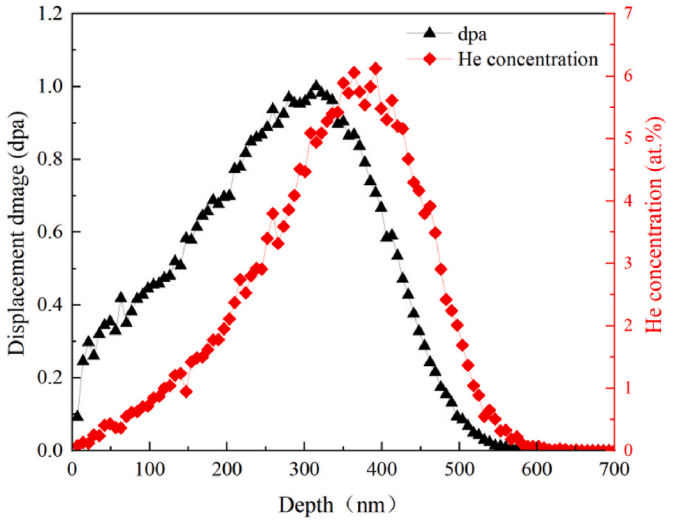


**Fig. 3.** The depth profiles of displacement damage and helium concentration simulated by SRIM software.

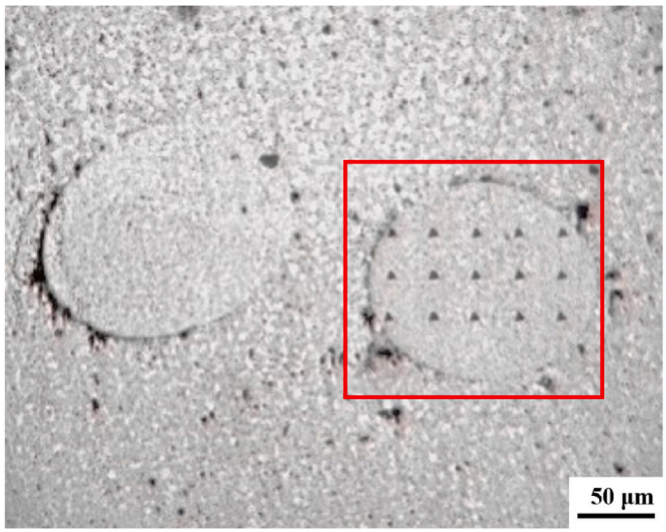


**Fig. 4.** Distribution of indentations in the W fiber after nanoindentation test.

the grazing incidence angle of the sample is assessed at 2°, eliminating the effect of the non-irradiated area. Samples for transmission electron microscope (TEM) observation were prepared by focused ion beam (FIB) conducted on a Helios NanoLab G3 UC SEM. TEM analysis was conducted using an AC-TEM (Titan Themis Z) with an acceleration voltage of 300 kV.

### 2.4. Nanoindentation

The nanoindentation test utilized the G200 universal nano-mechanical tester with a diamond Berkovich indenter. A continuous stiffness measurement method, characterized by a Poisson's ratio of ~0.3, a frequency of ~110 Hz, and an amplitude of ~2 nm [26], was employed to establish the correlation between indentation hardness and depth. Fig. 4 shows the distribution of indentations with spacing larger than 30 μm in the circle-shaped W fiber after nanoindentation test. The average hardness was calculated through the results of fifteen indentation tests. The nanoindentation experiments were carried out at room temperature.

## 3. Results

### 3.1. Microstructure of the $W_f$/W–$Y_2O_3$ composites before irradiation

Fig. 5 shows optical microstructure of the different $W_f$/W–$Y_2O_3$ composites before irradiation. As shown in Fig. 5a and b, the W fiber in the $W_f$/W–$Y_2O_3$ composites sintered at 1600 °C still show fine elongated grains. However, the W fiber in the $W_f$/W–$Y_2O_3$ composites sintered at 1800 °C show large coarse grains. It means that the W fiber is completely recrystallized, as shown in Fig. 5c and d. The W fiber without recrystallization and those completely recrystallized in the $W_f$/W–$Y_2O_3$ composites sintered at 1600 °C and 1800 °C are named as NRX-W fiber and RX-W fiber respectively. Different shapes of the short W fiber randomly

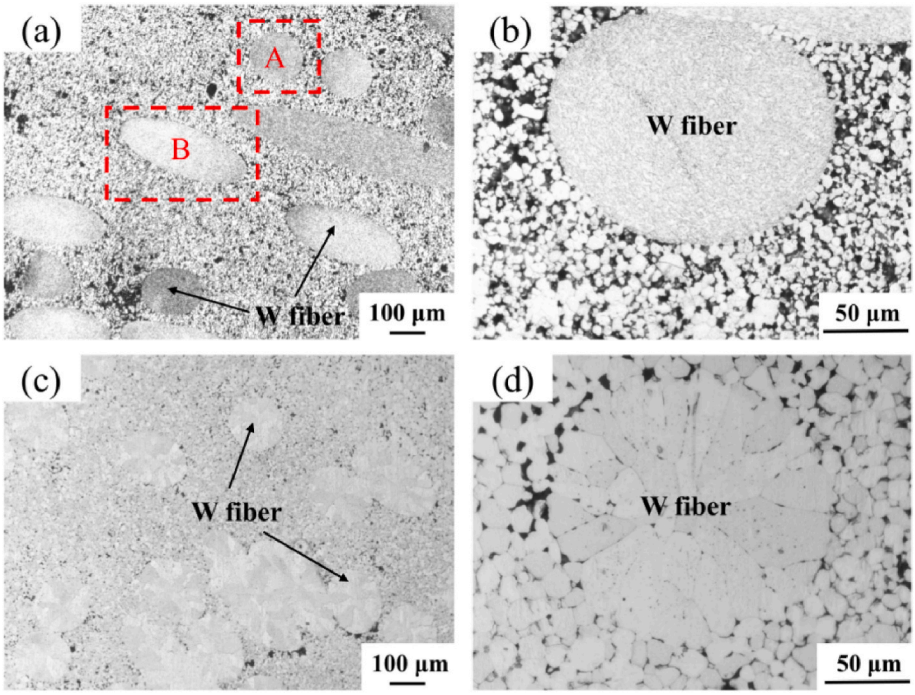


**Fig. 5.** (a) Low-magnification and (b) high-magnification optical micrographs of the $W_f/W–Y_2O_3$ composites sintered at 1600 °C. (c) Low-magnification and (d) high-magnification optical micrographs of the $W_f/W–Y_2O_3$ composites sintered at 1800 °C.

distributed in the composites can be seen, as marked in the region A and B of Fig. 5a. In order to avoid the effect of the orientation of the fiber, the irradiation hardening after helium ion irradiation was mainly investigated in the circle-shaped W fiber as marked in the region A.

The microstructure of the W fiber in these composites investigated by EBSD was shown in Fig. 6. The orientation maps of the NRX-W fiber and RX-W fiber before irradiation are illustrated in Fig. 6a and d, respectively. The NRX-W fiber has obvious {110} fiber texture along the axial direction. However, no obvious texture is observed in the W matrix. And the RX-W fiber in the composites sintered at 1800 °C did not show any

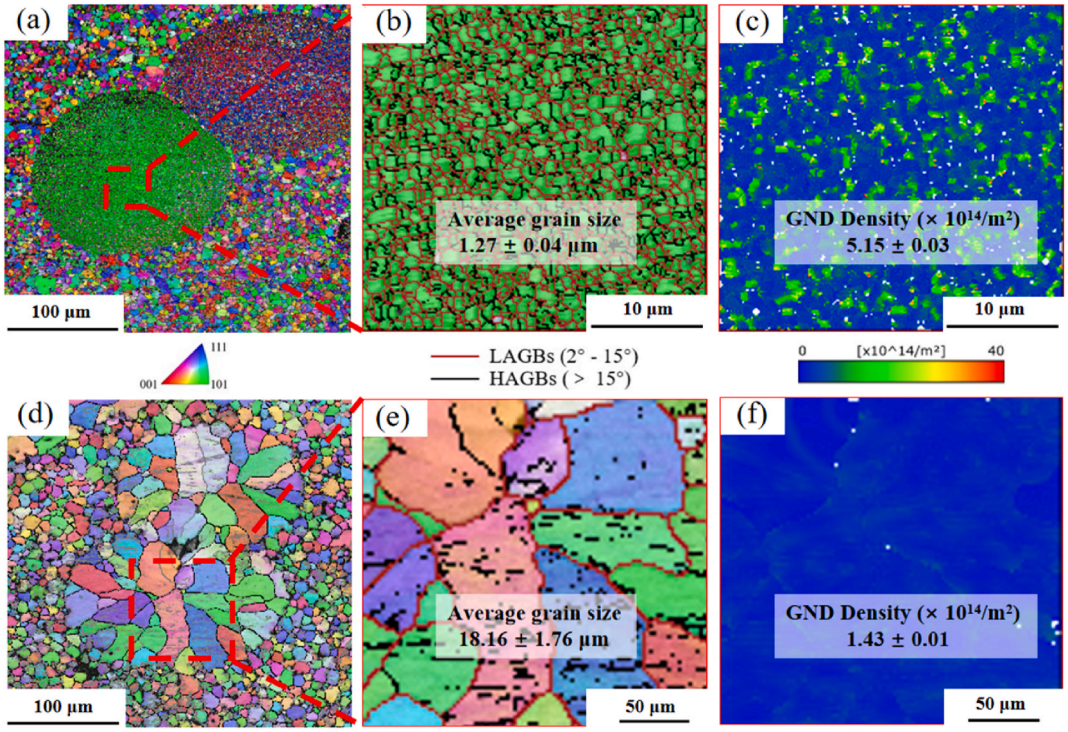


**Fig. 6.** EBSD maps showing the microstructure of NRX-W fiber and RX-W fiber in the $W_f/W–Y_2O_3$ composites respectively. (a) Orientation distribution map, (b) Orientation and grain boundary distribution map in the red region of (a), (c) GND density distribution map of the NRX-W fiber. (d) Orientation distribution map, (e) Orientation and grain boundary distribution map in the red region of (d). Red lines show LAGBs, and black lines show HAGBs. (f) GND density distribution map of the RX-W fiber.

obvious preferred orientation after complete recrystallization. According to the grain boundary misorientation distribution maps in Fig. 6b and e, a lot of low angle grain boundaries (LAGBs) have been remained in the NRX-W fiber. And the density of HAGBs in the W fiber of the RX-W sample is also lower, as shown in Fig. 7. In this study, the misorientation of the HAGBs is higher than 15°, and LAGBs mean the misorientation is between 2° and 15°. As shown in Fig. 6c and f, the density of geometrically necessary dislocations (GND) density in the RX-W fiber is obviously lower than that of the NRX-W fiber.

### 3.2. The microstructure evolution after ion irradiation

The GIXRD patterns of the $W_f/W–Y_2O_3$ composites sintered at 1600 °C and 1800 °C before and after helium ion irradiation are shown in Fig. 8a and c respectively. It can be seen that both the $W_f/W–Y_2O_3$ composites sintered at 1600 °C and 1800 °C have body-centered cubic (BCC) crystal structures with diffraction peaks of (110), (200), (211) and (220) respectively. No significant changes in the diffraction peaks were observed in the samples after irradiation, indicating that phase transformation did not occur in both the $W_f/W–Y_2O_3$ composites sintered at 1600 °C and 1800 °C after irradiation.

Due to the strong {110} texture along the axial direction of the NRX-W fiber, the difference of (110) peaks between the samples before and after irradiation was mainly analyzed in this study. The changes in the 2θ and full width at half maximum (FWHM) of (110) peak before and after irradiation for the W fiber in the $W_f/W–Y_2O_3$ composites are listed in Table 1. Fig. 8b and d shows the amplified peaks of the main diffraction peak (110) before and after irradiation for the composites sintered at 1600 °C and 1800 °C respectively. Compared to that of the non-irradiation samples, both the (110) peaks of the irradiated W fiber in the $W_f/W–Y_2O_3$ composites sintered at 1600 °C and 1800 °C showed a shift of the 2θ value towards a small angle as well as an increase of the FWHM. Both the observed diffraction peak shifts and broadening of the FWHM can be attributed to the irradiation-induced defects inducing lattice distortion. Specifically, the migration and accumulation of point defects induce lattice expansion accompanied by structural distortion (lattice strain), while the microscopic stress fields generated through defect interactions are further intensified by the formation of dislocation loops [27,28].

### 3.3. Distribution of irradiation-induced dislocation loops

Fig. 9 shows the TEM images investigating the microstructure of the NRX-W fiber and RX-W fiber after irradiation. In the NRX-W fiber, many fine subgrains can be seen in Fig. 9a. The average subgrain size is about 300 nm. In the subgrains, mainly two sets of long screw dislocations $b = 1/2 <111>$ forming as dislocation nets can be seen under zone axis [110], as shown in Fig. 9b. It can be concluded from these subgrains and dislocation nets that the W fiber was in a recovery condition, which is consistence with the EBSD results. Besides, dislocation loops are developed due to irradiation. For the RX-W fiber, no subgrains can be seen, as shown in Fig. 9d. However, planar high angle grain boundary can be seen. In these grains, few long dislocations can be seen, instead, mainly dislocation loops are formed.

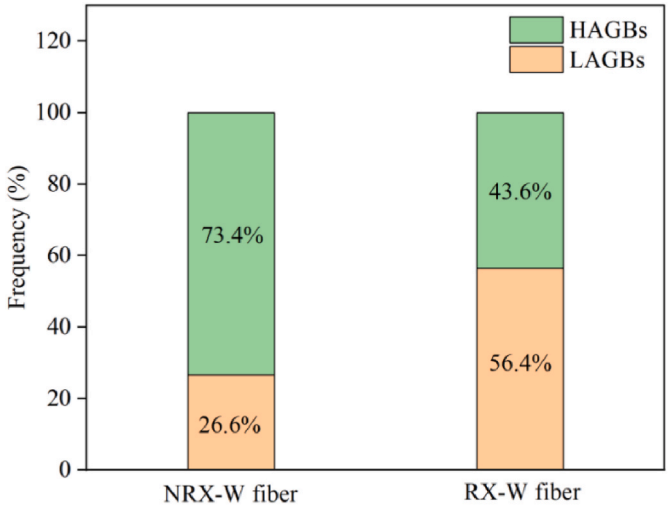


**Fig. 7.** Statistical diagram of the frequency of LAGBs and HAGBs inside the NRX-W fiber and RX-W fiber of the $W_f/W–Y_2O_3$ composites.

In order to investigate the density of dislocation loops in these two kinds of W fibers, three different $\vec{g}$ vectors, including $\vec{g_1} = [1\bar{1}\,0]$, $\vec{g_2} = [110]$ and $\vec{g_3} = [200]$ were conducted, as shown in Fig. 10. The observation area is near the same under different $\vec{g}$ vectors.

The density and size distribution of the dislocation loops in the NRX-W fiber and RX-W fiber captured under three kinds of $\vec{g}$ vectors are shown in Fig. 11. For the NRX-W fiber, the number densities of dislocation loops captured in two equivalent $\vec{g}$ vectors, $\vec{g_1} = [1\,\bar{1}\,0]$, $\vec{g_2} = [110]$, are $0.7 \times 10^{23}$ m$^{-3}$ and $0.8 \times 10^{23}$ m$^{-3}$, and the size are $3.4 \pm 0.7$ nm and $3.3 \pm 0.7$ nm. The number density and size of dislocation loops captured in $\vec{g_3} = [200]$ are $4.0 \pm 0.6$ nm and $1.5 \times 10^{23}$ m$^{-3}$. For the RX-W fiber, the number densities of dislocation loops captured in $\vec{g_1} = [1\,\bar{1}\,0]$ and $\vec{g_2} = [110]$ are $1.1 \times 10^{23}$ m$^{-3}$ and $1.2 \times 10^{23}$ m$^{-3}$; the size are $4.0 \pm 0.6$ nm and $4.2 \pm 0.7$ nm. The number density and size of dislocation loops captured in $\vec{g_3} = (200)$ are $5.1 \pm 0.6$ nm and $2.3 \times 10^{23}$ m$^{-3}$.

The main types of irradiation-induced dislocation loops in tungsten irradiated with helium ions at room temperature are the $b = <100>$ and $b = 1/2 <111>$ types [29]. The statistical dislocation extinction conditions are shown in Table 2. The $b = <100>$-type loop under the $\vec{g_2} = [110]$ vector has a 1/3 probability of diffraction extinction, and the $b = 1/2 <111>$-type dislocations have a 1/2 probability of diffraction extinction. The $b = <100>$-type dislocations calculated under the $\vec{g_3} = [200]$ vector has a 2/3 probability of diffraction extinction, and the $b = 1/2 <111>$-type dislocations do not appear diffraction extinction. Therefore, the ratio of the two types of dislocation loops in NRX-W fiber and RX-W fiber can be estimated by Eqs. (1) and (2).

$$\rho_{(g=[110])} = 2/3\rho_{(b=<100>)} + 1/2\rho_{(b=1/2<111>)} \quad (1)$$

$$\rho_{(g=[200])} = 1/3\rho_{(b=<100>)} + \rho_{(b=1/2<111>)} \quad (2)$$

where $\rho_{(g=[110])}$ represents the density of dislocations counted under $\vec{g_1} = [110]$, $\rho_{(g=[200])}$ represents the density of dislocations counted under $\vec{g_3} = [200]$, $\rho_{(b=<100>)}$ represents the density of $b = <100>$-type dislocations, $\rho_{(b=1/2<111>)}$ represents the density of $b = 1/2 <111>$-type dislocations.

The actual number densities of dislocation loops estimated under different g-vectors are shown in Table 3. The results show that the Burgers vector of dislocation loops produced in the NRX-W fiber and RX-W fiber after helium ion irradiation are mainly $b = 1/2 <111>$-type, and a few of dislocation loops are $b = <100>$-type.

### 3.4. Irradiation-induced hardening

Fig. 12a illustrates the relationship between the measured hardness and the indentation depth of the W fiber in both non-irradiated and irradiated composites. It is evident that a significant influence on the hardness of the W fiber was observed after He ion irradiation. According to the Nix-Gao model [30], the occurrence of the indentation size effect (ISE) results in a gradual reduction of nanoindentation hardness as the depth increases. The hardness ($H_0$) can be calculated by Eq. (3).

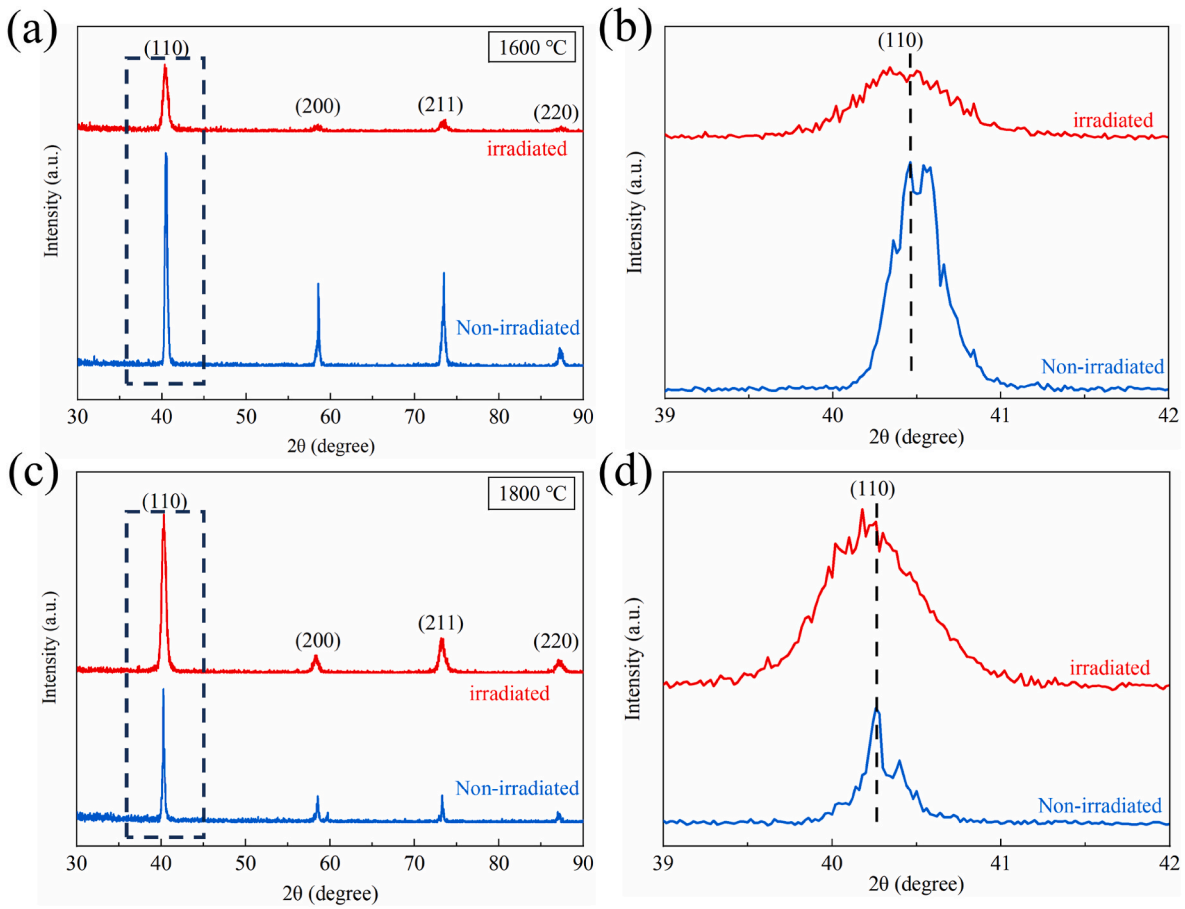


**Fig. 8.** GIXRD patterns of the different $W_f$/W–$Y_2O_3$ composites before and after irradiation. (a) Sintered at 1600 °C; (b) Magnification of the (110) peak in (a). (c) Sintered at 1800 °C; (d) Magnification of the (110) peak in (c).

**Table 1**
The 2θ and the FWHM of (110) peaks for the NRX-W fiber and RX-W fiber before and after irradiation.

| Samples | NRX-W fiber | | RX-W fiber | |
|---|---|---|---|---|
| | Non-irradiated | Irradiated | Non-irradiated | Irradiated |
| 2θ (°) | 40.460 | 40.340 | 40.259 | 40.181 |
| FWHM (°) | 0.308 | 0.532 | 0.195 | 0.536 |

$$H^2 = H_0{}^2\left(1+\frac{h^*}{h}\right) \tag{3}$$

Where H is the measured nanoindentation hardness value, h is the indentation depth, and h* is a parameter representing the response to the ISE with dimensional length. As shown in Fig. 12b, linear relation can be obtained between the square of nanoindentation hardness ($H^2$) and the reciprocal of the indentation depth (1/h). Since the difference in the hardness (denoted as ΔH) between non-irradiated and irradiated W fiber has been evaluated, the ISE of the sample is fundamentally equivalent both before and after irradiation.

The difference in the hardness of the W fiber before and after irradiation is shown in Table 4. Before irradiation, the hardness of NRX-W fiber is 8.27 ± 0.04 GPa, which is higher than that of the RX-W fiber (5.98 ± 0.04 GPa) due to the lower dislocation density in the RX-W fiber before irradiation. After He ion irradiation, the NRX-W fiber is 12.65 ± 0.14 GPa, while that of the RX-W fiber is 11.06 ± 0.21 GPa. It means that both the NRX-W fiber and RX-W fiber in the composites exhibit significant hardening after helium ion irradiation. For the difference in hardness (denoted as ΔH) between non-irradiated and irradiated conditions, the NRX-W fiber exhibits a hardness increment of approximately 4.38 ± 0.10 GPa. And the RX-W fiber has a higher hardness increment of about 5.08 ± 0.17 GPa. Meanwhile, the irradiation hardening rates of the NRX-W fiber and RX-W fiber differ significantly, which are 52.96 % and 84.95 %, respectively.

## 4. Discussion

### *4.1. The effect of the initial microstructure on dislocation loops of the W fiber*

Whether it is the NRX-W fiber or RX-W fiber, the number densities and size of dislocation loops at the equivalent g vectors are approximately equal, which indicates that the dislocation loops of both are uniformly distributed in the equivalent crystallographic direction. Meanwhile, regarding the differences in the distribution of dislocation loops between the two kinds of W fibers, the number density and size of dislocation loops of RX-W fiber under the same g vector are both greater than those of NRX-W fiber. This is mainly due to the differences in defect evolution during irradiation. Energetic particle irradiation generates point defects (vacancy-interstitial atom pairs) and their clusters (such as dislocation loops), which hinder dislocation movement and lead to hardening. These defects will subsequently undergo recombination or migration to defect traps (such as grain boundaries, dislocation lines and phase interfaces) through the overheat activation process. The number of residual defects is affected by temperature, defect mobility and trap density/distribution. In this study, the NRX-W fiber has obvious {110} fiber texture, a smaller grain size, a larger proportion of HAGBs, and a higher GND density. The different orientations of grains in W have no

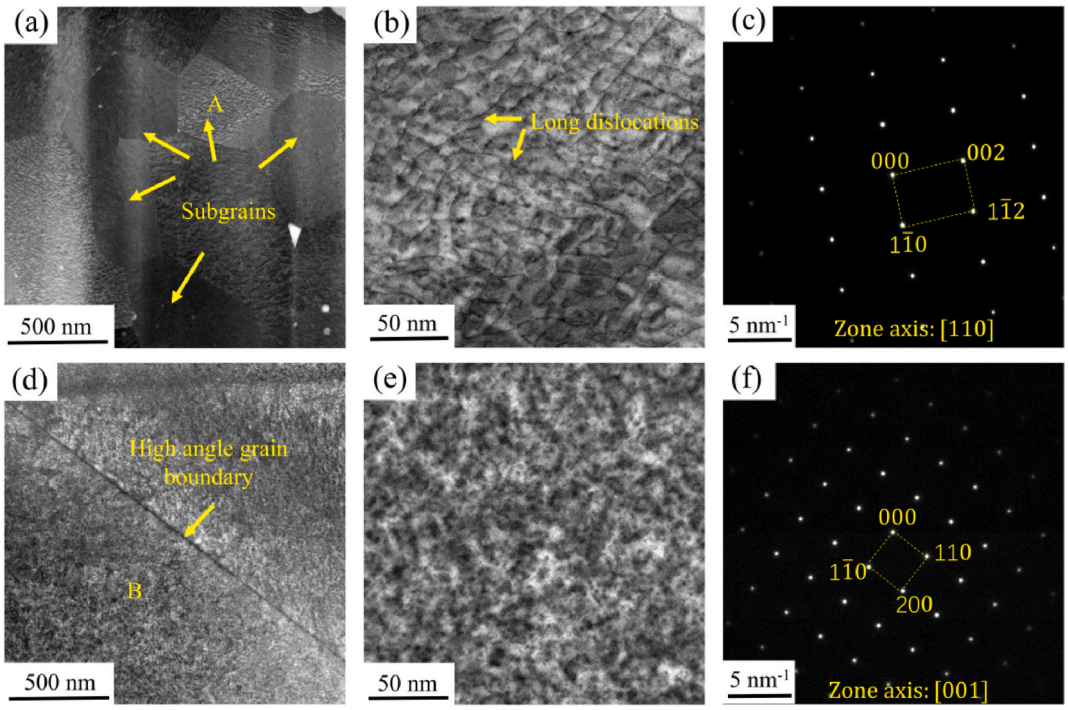


**Fig. 9.** TEM images showing the microstructure of (a, b and c) the NRX-W fiber and (d, e and f) RX-W fiber after irradiation. (a) The subgrains, (b) the dislocations in subgrain A and (c) the corresponding selected area diffraction patterns (SADPs) of subgrain A, the zone axis is [110]. (d) The grains, (e) the dislocation loops in grain B and (f) the corresponding SADPs of the grain B, the zone axis is [100].

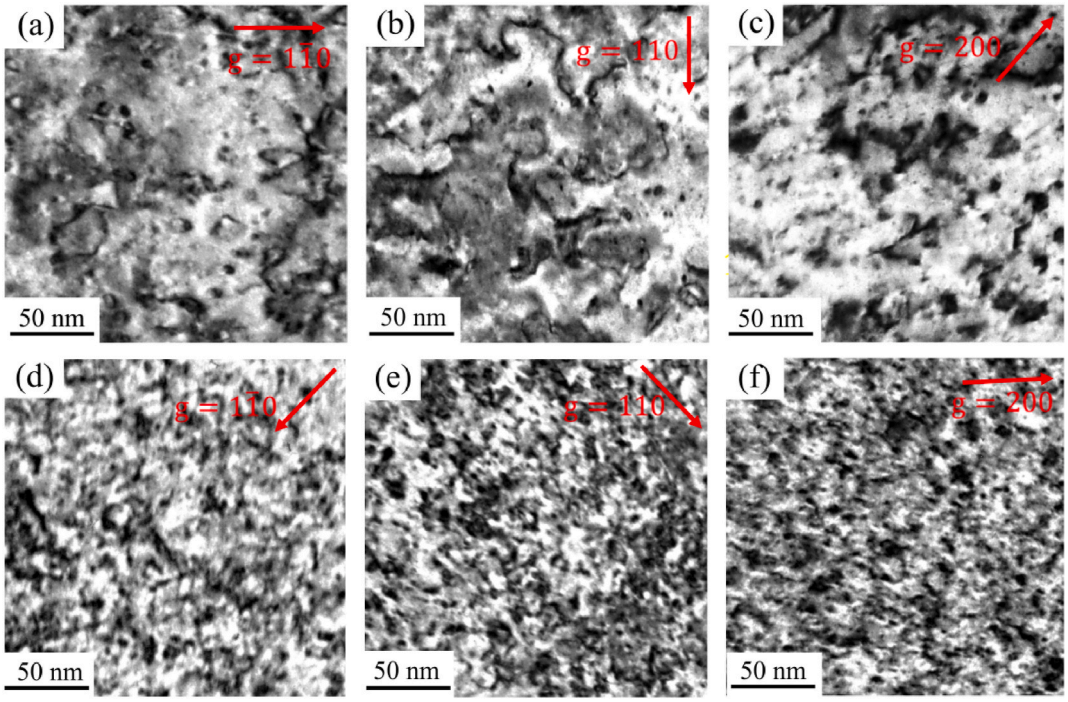


**Fig. 10.** Dislocation loops of the NRX-W fiber and RX-W fiber under three different $\vec{g}$ vectors after He irradiation: (a) $\vec{g_1}$ = [1 $\bar{1}$ 0], (b) $\vec{g_2}$ = [110] and (c) $\vec{g_3}$ = [200] of the dislocation loops in the NRX-W fiber. (d) $\vec{g_1}$ = [1 $\bar{1}$ 0], (e) $\vec{g_2}$ = [110] and (f) $\vec{g_3}$ = [200] of the dislocation loops in the RX-W fiber.

significant difference in their influence on the evolution of dislocation loops [31]. Smaller grain size means it has higher-density grain boundaries, which can serve as defect sinks after irradiation [32]. The HAGBs are generally considered as better defect sinks than LAGBs due to the higher energy. Meanwhile, the initial GND can inhibit the formation of irradiation-induced defects [33]. For the type of dislocation loops, compared with the RX-W fiber, the proportion of 1/2 <111>-type dislocation loops produced by the NRX-W fiber has decreased significantly, while the proportion of <100>-type dislocation loops shows little difference. This might be due to the fact that a large number of 1/2 <111>-type dislocation loops (with higher mobility) have been annihilated on the pre-existing dislocation lines [34].

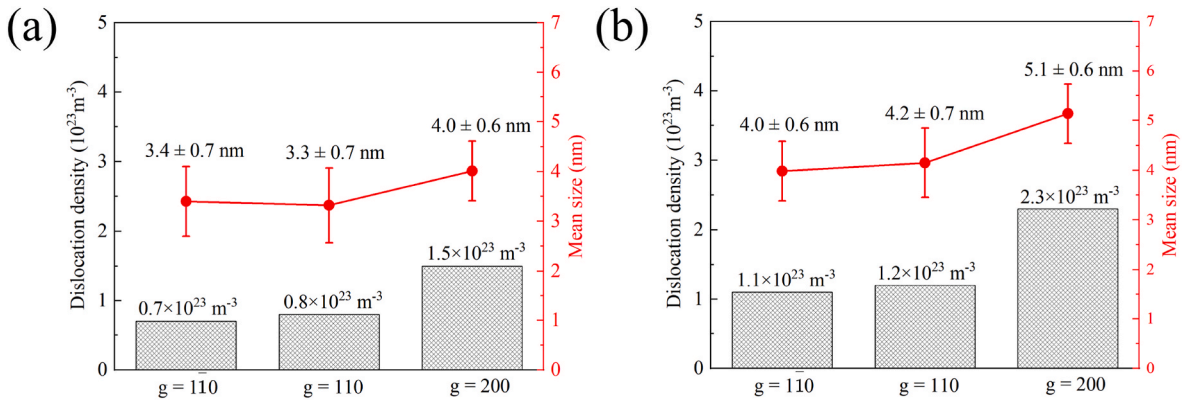


**Fig. 11.** The density and size of dislocation loops under three different *g*-vectors for (a) the NRX-W fiber and (b) the RX-W fiber.

**Table 2**
The dislocation types in tungsten under different *g*-vectors.

| *g*/ *b* | [100] | [010] | [001] | 1/2 [111] | 1/2[$\bar{1}$ 11] | 1/2[1 $\bar{1}$ 1] | 1/2[11 $\bar{1}$ $\bar{}$] |
|---|---|---|---|---|---|---|---|
| [110] | ✓ | ✓ | × | ✓ | × | × | ✓ |
| [200] | ✓ | × | × | ✓ | ✓ | ✓ | ✓ |

**Table 3**
The number density of dislocation loops in the NRX-W fiber and RX-W fiber ($10^{23}$m$^{-3}$).

| Samples | Dislocation Loops Under Different *g*-Vectors | | Different Types of Dislocation Loops | | Total |
|---|---|---|---|---|---|
| | *g* = [110] | *g* = [200] | *b* = <100> | *b* = 1/2<111> | |
| NRX-W fiber | 0.8 | 1.5 | 0.1 | 1.5 | 1.6 |
| RX-W fiber | 1.2 | 2.3 | 0.1 | 2.3 | 2.4 |

### *4.2. The effect of the initial microstructure on irradiation hardening of the W fiber*

Irradiation hardening is due to irradiation-induced defects such as dislocation loops hindering the movement of dislocations during the nanoindentation process. Generally, the contribution of dislocation loops to irradiation hardening can be described by the dispersed barrier hardening (DBH) model as Eq. (4) [35].

$$\Delta\sigma = M\alpha'\mu b\sqrt{Nd} \tag{4}$$

where Δσ is the increase of yield stress, N and d are the number density and size of dislocation loops, M = 3.0 is the Taylor factor, μ = 160 GPa is the shear modulus, *b* = 0.28 nm is burgers vector of dislocation and adequate value of α'is 0.33 for dislocation loops [35].

Theoretically, the corresponding relationship between the hardness change (ΔH) before and after irradiation measured by nanoindentation and the change in yield stress follow Eq. (5) [36].

$$\Delta\sigma = 289\Delta H \tag{5}$$

The irradiation hardening of the NRX-W fiber and RX-W fiber calculated by the DBH model was 3.68 GPa and 4.99 GPa, respectively. The theoretical value calculated by the DBH model is slightly lower than the experimental value. It can be seen that the dislocation loops are directly related to the irradiation hardening of the NRX-W fiber and RX-

**Table 4**
The hardness obtained by the Nix-Gao model fitting (ΔH indicates the difference in the hardness before and after irradiation).

| Samples | NRX-W fiber | RX-W fiber |
|---|---|---|
| $H_{unirr}$ (GPa) | 8.27 ± 0.04 | 5.98 ± 0.04 |
| $H_{irr}$ (GPa) | 12.65 ± 0.14 | 11.06 ± 0.21 |
| ΔH (GPa) | 4.38 ± 0.10 | 5.08 ± 0.17 |
| Hardening rate (%) | 52.96 | 84.95 |

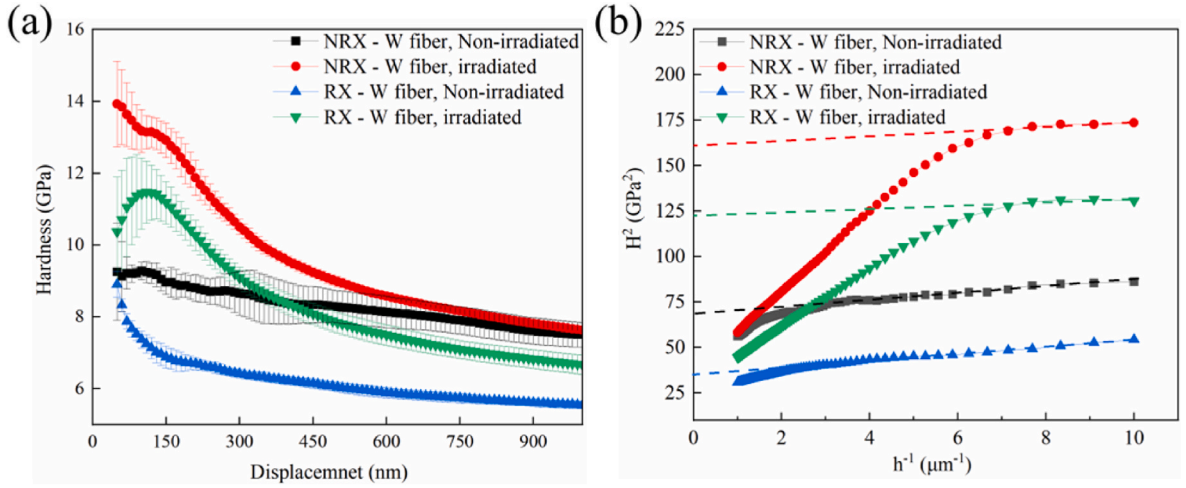


**Fig. 12.** Plots of hardness for the NRX-W fiber and RX-W fiber before and after irradiation. (a) Average hardness versus the indentation depth of the W fiber. (b) Curves of $H^2$ - 1/h for the average hardness of the W fiber.

W fiber.

Considering the significant difference in crystal orientation between the NRX-W fiber and RX-W fiber, the initial microstructure and irradiation hardening of the non-circular NRX-W fiber in the sample sintered at a temperature of 1600 °C, as shown in region B of Fig. 5a, were studied. As shown in Fig. 13a, no < 110> preferred orientation was favored within the non-circular NRX-W fiber, which is different from the <110> texture of the circular NRX-W fiber. However, the grain size, GND density and the proportion of HAGBs were similar in these non-circular and circular NRX-W fiber. Therefore, the main difference between the two types of W fibers lies in the different orientations of the internal grains.

Fig. 14 shows the nano-indentation test results of non-circular NRX-W fiber and RX-W fiber. The hardness of non-circular NRX-W fiber before and after irradiation was 8.47 ± 0.07 GPa and 11.93 ± 0.17 GPa, respectively. The irradiation hardening increment and hardening rate were 3.46 ± 0.10 GPa and 40.85 %, respectively. This result was slightly lower than that of circular NRX-W fiber (4.38 ± 0.10 GPa and 52.96 %). However, for the non-circular RX-W fiber, the hardness before and after irradiation was 5.90 ± 0.04 GPa and 11.13 ± 0.20 GPa, respectively. The irradiation hardening increment and hardening rate were 5.23 ± 0.16 GPa and 88.64 %, respectively. This result is almost identical to the circular RX-W fiber (5.08 ± 0.17 GPa and 84.95 %). The initial microstructure of non-circular and circular RX-W fiber is similar because they are equiaxed grains and without obvious texture. These results indicate that the crystal orientation within the W fiber has a relatively minor effect on irradiation hardening. Therefore, compared to the influence of crystal orientation on the irradiation hardening of W fiber, the initial higher subgrain boundaries and GND density in NRX-W fiber play a dominant role in the irradiation hardening process, ultimately resulting in a higher irradiation hardening rate in RX-W fiber.

The significant difference in irradiation hardening between the NRX-W fiber and RX-W fiber fundamentally arises from the distinct role dislocation loops play as barriers to dislocation glide, the primary mechanism of plastic deformation. Dislocation loops, formed during irradiation, act as strong obstacles that impede the motion of mobile dislocations through the crystal lattice. This obstruction necessitates an increased applied stress (the hardening increment, ΔH) to force dislocations past or around these loops, primarily governed by mechanisms like Orowan looping for larger loops or cutting for smaller ones [37]. The DBH model quantitatively captures this effect by treating the loops as obstacles characterized by their strength. The experimental observations by TEM (Fig. 10) provide direct evidence for this microstructural origin of the hardening difference. The TEM micrographs reveal that the RX-W fiber developed a markedly higher density of dislocation loops alongside larger average loop sizes compared to the NRX-W fiber following helium ion irradiation. This pronounced contrast in loop characteristics directly translates to a higher density of strong obstacles within the RX-W fiber. Consequently, mobile dislocations in the RX-W fiber encounter significantly greater resistance to their motion, requiring a higher stress (manifested as 4.99 GPa hardening) to induce plastic flow, consistent with the DBH model prediction. Conversely, the initially higher density of HAGBs, subgrain boundaries, and GNDs in the NRX-W fiber provided efficient sinks for irradiation-induced point defects (vacancies and interstitials). This enhanced defect annihilation capability effectively suppressed the nucleation and growth of dislocation loops within the grain interiors of NRX-W fiber, resulting in a lower obstacle density and smaller loop sizes. Consequently, mobile dislocations in the NRX-W fiber experience less impediment, leading to the lower observed hardening (3.68 GPa). Therefore, the DBH model's prediction of higher hardening in the RX-W fiber is mechanistically underpinned by its greater population of larger dislocation loops, acting as more formidable obstacles, a conclusion directly supported by the TEM analysis.

From the above analysis, it can be seen that the initial microstructure has an important effect on the irradiation hardening of the W fiber in the $W_f$/W–$Y_2O_3$ composites. Based on this finding, the helium ion irradiation hardening resistance of the W fiber can be improved by controlling these conditions. Meanwhile, the recrystallization of W fiber in the $W_f$/W composites will reduce the service life in the irradiation environment. Therefore, measures should be taken to suppress the recrystallization phenomenon of W fiber in the composites during the sintering process.

## 5. Conclusions

In this study, the microstructure evolution and irradiation hardening of the W fiber with different microstructures for $W_f$/W–$Y_2O_3$ composites sintered at 1600 °C and 1800 °C were investigated after irradiation with 180 keV He ions at room temperature. The following conclusions are obtained.

(1) The crystal structures of the $W_f$/W–$Y_2O_3$ composites sintered at 1600 °C and 1800 °C are still body-centered cubic (BCC) structures after irradiation with He ions. However, both of them show lattice distortion and microscopic stress, resulting in the left shift of the diffraction peak 2θ and the increase of FWHM.

(2) The results of nanoindentation showed that both the NRX-W fiber and the RX-W fiber underwent significant helium ion irradiation hardening. The irradiation hardening increment of NRX-W fiber was 4.38 ± 0.10 GPa, slightly lower than that of RX-W fiber (5.08 ± 0.17 GPa). However, the hardening rate of NRX-W fiber was 52.96 %, which was significantly different from that of RX-W fiber (84.95 %). It means that NRX-W fiber in the composites has a stronger resistance to helium ion irradiation hardening.

(3) Compared with the RX-W fiber, the initial larger proportion of HAGBs, higher density of subgrain boundaries and GND in the

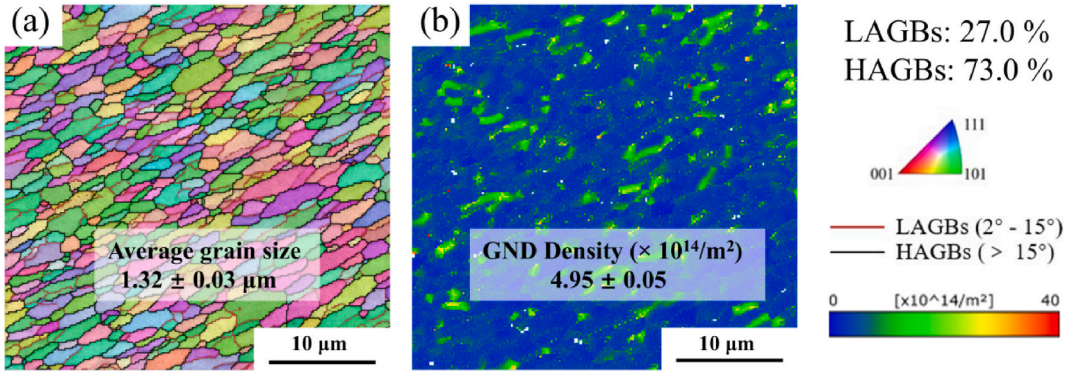


**Fig. 13.** EBSD maps showing the microstructure of non-circular NRX-W fiber in the $W_f$/W–$Y_2O_3$ composites. (a) Orientation and grain boundary distribution map, (b) GND density distribution map of the non-circular NRX-W fiber.

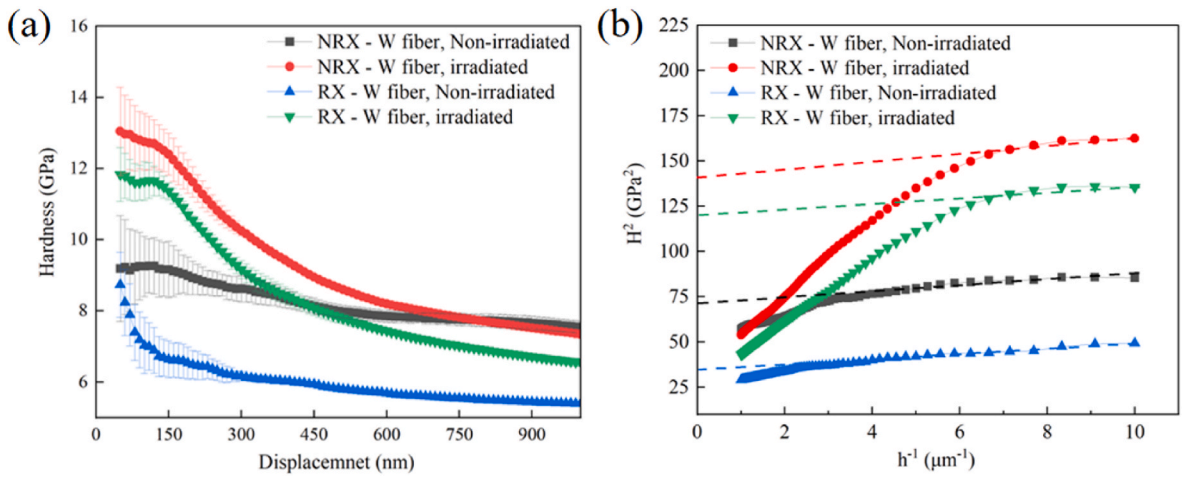


**Fig. 14.** Plots of hardness for the non-circular NRX-W fiber and RX-W fiber before and after irradiation. (a) Average hardness versus the indentation depth of the W fiber. (b) Curves of $H^2$ - 1/h for the average hardness of the W fiber.

NRX-W fiber significantly inhibit the nucleation and growth of irradiation-induced dislocation loops by enhancing the defect capture ability. This leads to the dislocation loops produced in the NRX-W fiber having a smaller number density and size.

(4) The dislocation loops in the NRX-W fiber and RX-W fiber are uniformly distributed in the equivalent crystallographic orientation. The theoretical irradiation hardening values of NRX-W fiber and RX-W fiber calculated by the DBH model were 3.68 GPa and 4.99 GPa respectively, which were slightly lower than the experimental values. It can be seen that the dislocation loops make a dominant contribution to the irradiation hardening of NRX-W fiber and RX-W fiber.

## Data availability

The raw data related to this manuscript would be made available on request.

## Declaration of competing interest

The authors declared that they have no conflicts of interest to this work. We declare that we do not have any commercial or associative interest that represents a conflict of interest in connection with the work submitted.

## Acknowledgments

This work is supported by Anhui Provincial Natural Science Foundation (2308085ME134), National Natural Science Foundation of China (12205070, 12205071), the Fundamental Research Funds for the Central Universities (PA2024GDGP0042).

## References

[1] Riesch J, Han Y, Almanstötter J, Coenen JW, Höschen T, Jasper B, Zhao P, Linsmeier Ch, Neu R. Development of tungsten fibre-reinforced tungsten composites towards their use in DEMO—potassium doped tungsten wire. Phys Scripta 2016:014006. 1-8.

[2] Zhang H, Jiang Y, Fang QF, Xie ZM, Miao S, Zeng LF, Zhang T, Wang XP, Liu CS. Microstructure and mechanical properties of tungsten composite reinforced by fibre network. Front Mater Sci 2017;11:190–6.

[3] Yan F, Liu ZT, Liu WT. Structural and optical properties of yttrium trioxide thin films prepared by RF magnetron sputtering. Vacuum 2011;86:72.

[4] Bose PP, Gupta MK, Mittal R, Rols S, Achary SN, Tyagi AK, Chaplot SL. Phase transitions and thermodynamic properties of yttria, $Y_2O_3$: inelastic neutron scattering shell model and first-principles calculations. Phys Rev B 2011;84:094301.

[5] Mao YR, Engels J, Houben A, Rasinski M, Steffens J, Terra A, Linsmeier Ch, Coenen JW. The influence of annealing on yttrium oxide thin film deposited by reactive magnetron sputtering: process and microstructure. Nucl Mater Energy 2017;10:1–8.

[6] Forrest R, Tabasso A, Danani C, Jakhar S, Shaw A. In: Handbook of activation data calculated using EASY-2007. UKAEA FUS; 2009. p. 552.

[7] Mao YR, Coenena JW, Riesch J, Sistlac S, Almanstötter J, Jasper B, Terra A, Höschen T, Gietl H, Linsmeiera Ch, Broeckmann C. Influence of the interface strength on the mechanical properties of discontinuous tungsten fiber-reinforced tungsten composites produced by field assisted sintering technology. Compos Part A 2018;107:342–53.

[8] Barabash V, , The ITER International Team, Peacock A, Fabritsiev S, Kalinin G, Zinkle S, Rowcliffe A, Rensman J-W, Tavassoli AA, Marmy P, Karditsas PJ, Gillemot F, Akiba M. Materials challenges for ITER – current status and future activities. J Nucl Mater 2007;367–370:21–32.

[9] Steichen JM. Tensile properties of neutron irradiated TZM and tungsten. J Nucl Mater 1976;60:13–9.

[10] Maloy SA, James MR, Sommer Jr W, Willcutt Jr GJ, Lopez M, Romero TJ, Toloczko MB. The effect of 800 MeV proton irradiation on the mechanical properties of tungsten at room temperature and at 475 °C. J Nucl Mater 2005;343:219–26.

[11] Chen C, Chen Y, Han X, Li KL, Wang S, Zhang YF, Mao YR, Coenen JW, Wang J, Luo LM. Microstructure and failure mechanism of $Y_2O_3$ coating on the W fiber in $W_f$/W composites during field assisted sintering. J Mater Res Technol 2024;30:8661–70.

[12] Gietl H, Olbrich S, Riesch J, Holzner G, Höschen T, Coenen JW, Neu R. Estimation of the fracture toughness of tungsten fibre-reinforced tungsten composites. Eng Fract Mech 2020;232:107011.

[13] Shu R, Mao YR, Coenen JW, Terra A, Liu C, Schonen S, Riesch J, Linsmeier C, Broeckmann C. Interface and mechanical properties of the single-layer long fiber reinforced Wf/W-Y2O3 composites fabricated via field assisted sintering technology. Mater Sci Eng, A 2022;857:144098.

[14] Mao YR, Duggal A, Dittes A, Lampke T, Coenen JW, Linsmeier Ch. Electrophoretic deposition prepared yttria as interface of tungsten fiber reinforced tungsten composites. Nucl Mater Energy 2023;36:101487.

[15] Chen C, Chen Y, Li KL, Wang S, Zhang YF, Mao YR, Coenen JW, Wang J, Luo LM, Wu YC. Interfacial microstructure and mechanical property of the discontinuous short tungsten fiber-reinforced tungsten matrix composites. Mater Char 2024;215:114214.

[16] Chen Y, Chen C, Chen JH, Li KL, Wang S, Zhang YF, Chen HY, Beri TH, Wang J, Luo LM, Wu YC. The effect of $Y_2O_3$ particles on the microstructure and mechanical properties of tungsten fiber-reinforced tungsten composites. Mater Sci Eng, A 2024;918:147449.

[17] Hu X, Koyanagi T, Fukuda M, Kiran Kumar NAP, Snead LL, Wirth BD, Katoh Y. Irradiation hardening of pure tungsten exposed to neutron irradiation. J Nucl Mater 2016;480:235–43.

[18] Kohyama A, Katoh Y, Ando M, Jimbo K. A new Multiple Beams–Material Interaction Research Facility for radiation damage studies in fusion materials. Fusion Eng Des 2000;51–52:789–95.

[19] Serruys Y, Ruault M-O, Trocellier P, Miro S, Barbu A, Boulanger L, Kaïtasov O, Henry S, Leseigneur O, Trouslard Ph, Pellegrino S, Vaubaillon S. JANNUS: experimental validation at the scale of atomic modelling. CRPhys 2008;9:437–44.

[20] El-Atwani O, Esquivel E, Efe M, Aydogan E, Wang YQ, Martinez E, Maloy SA. Loop and void damage during heavy ion irradiation on nanocrystalline and coarse grained tungsten: microstructure, effect of dpa rate, temperature, and grain size. Acta Mater 2018;149:206–19.

[21] Zhang ZX, Chen DS, Han WT, Kimura A. Irradiation hardening in pure tungsten before and after recrystallization. Fusion Eng Des 2015;98–99:2103–7.

[22] Yao G, Tan XY, Fu MQ, Luo LM, Zan X, Xu Q, Liu JQ, Zhu XY, Cheng JG, Wu YC. Isotropic thermal conductivity in rolled large-sized W-Y2O3 bulk material prepared by powder metallurgy route and rolling deformation technology. Fusion Eng Des 2018;137:325–30.
[23] Ziegler JF. The stopping and range of ions in matter. Elsevier Science & Technology Books; 1985.
[24] Sigmund P. A note on integral equations of the Kinchin-Pease type. Radiat Eff 1969;1:15–8.
[25] ASTM Standard E 521. Standard practice for neutron radiation damage simulation by charged-particle irradiation. West Conshock-en, PA: ASTM International; 1996.
[26] Oliver WC, Pharr GM. Measurement of hardness and elastic modulus by instrumented indentation: advances in understanding and refinements to methodology. J Mater Res 2004;19:3–20.
[27] Javadi S, Ouyang B, Zhang Z, Ghoranneviss M, Salar Elahi A, Rawat RS. Effects of fusion relevant transient energetic radiation, plasma and thermal load on PLANSEE double forged tungsten samples in a low energy plasma focus device. Appl Surf Sci 2018;443:311–20.
[28] Nappé JC, Monnet I, Grosseau Ph, Audubert F, Guilhot B, Beauvy M, Benabdesselam M, Thomé L. Structural changes induced by heavy ion irradiation in titanium silicon carbide. J Nucl Mater 2011;409:53–61.
[29] Ding Y, Guo L, Li Y, Liu X, Ran G, Wu L, Qiu X, Deng H, Wu X, Li Y, Huang X. In-situ TEM observation and MD simulation of the reaction and transformation of <100> loops in tungsten during $H_2^+$ & $He^+$ dual-beam irradiation. Scr Mater 2021;204:114154.
[30] Nix WD, Gao HJ. Indentation size effects in crystalline materials: a law for strain gradient plasticity. J Mech Phys Solid 1998;46(3):411–25.
[31] Yin C, Bonny G, Terentyev D. Anisotropy in the hardness of single crystal tungsten before and after neutron irradiation. J Nucl Mater 2021;546:152759.
[32] Wei J, Feng B, Tochigi E, Shibata N, Ikuhara Y. Direct imaging of the disconnection climb mediated point defects absorption by a grain boundary. Nat Commun 2022;13:1455.
[33] Oh Y, Sung S, Jang J-i, Ko W-S, Han HN. Integrated experimental and computational study on the effect of hydrogen in mechanical responses of pure tungsten. Acta Mater 2024;280:120341.
[34] Li YP, Wang L, Ran G, Yuan Y, Wu L, Liu XY, Qiu X, Sun ZP, Ding YF, Han Q, Wu XY, Deng HQ, Huang XY. In-situ TEM investigation of 30 keV $He^+$ irradiated tungsten: effects of temperature, fluence, and sample thickness on dislocation loop evolution. Acta Mater 2021;206:116618.
[35] Meyers MA. Mechanical behavior of materials. Cambridge: Cambridge University Press; 2009 [Chapter 4]: Imperfections: Point and Line Defects.
[36] Krumwiede DL, Yamamoto T, Saleh TA, Maloy SA, Odette GR, Hosemann P. Direct comparison of nanoindentation and tensile test results on reactor-irradiated materials. J Nucl Mater 2018;504:135–43.
[37] Proville L, Bakó B. Dislocation depinning from ordered nanophases in a model fcc crystal: from cutting mechanism to Orowan looping. Acta Mater 2010;58:5565–71.